Hindawi
Advances in Meteorology
Volume 2024, Article ID 4509221, 19 pages
https://doi.org/10.1155/2024/4509221

Research Article

Analysis of Urban Heat Island Effect in Wuhan Urban Area Based on Prediction of Urban Underlying Surface Coverage Type Change

Wanyi Zuo,[1] Zhigang Ren,[1,2] Xiaofang Shan,[1,2] Zeng Zhou,[3] and Qinli Deng [1,2]

[1]*School of Civil Engineering and Architecture, Wuhan University of Technology, Wuhan 430070, China*
[2]*Hainan Institute of Wuhan University of Technology, No. 5 Chuangxin Road, Sanya 572024, China*
[3]*School of Urban Design, Wuhan University, 8 Donghu Nan Road, Wuhan, Hubei 430072, China*

Correspondence should be addressed to Qinli Deng; deng4213@whut.edu.cn

Received 4 January 2024; Revised 25 March 2024; Accepted 1 April 2024; Published 22 April 2024

Academic Editor: Stefania Bonafoni

The rapid development of urbanization makes the phenomenon of urban heat islands even more serious. Predicting the impact of land cover change on urban heat island has become one of the research hotspots. Taking Wuhan, China, as an example, this study simulated the land type change in 2020 through the Cellular Automata-Markov-Chain (CA-Markov) model. The urban heat island in 2020 was simulated and analyzed in conjunction with the Weather Research & Forecasting Model (WRF), and the simulation results of wind velocity and temperature were confirmed using weather station observation data. Based on this, the land cover and urban heat island of Wuhan in 2030 were predicted. The temperature was found to be well-fit by CA-Markov simulated land use data, with an average inaccuracy of about 2.5°C for weather stations. Wind speed had a poor fitting effect; the average error was roughly 2 m/s. The built-up area was the center of the high temperature area both before and after the prediction, the water was the low temperature area, and the peak heat island happened at night. According to the forecast results, there will be more built-up land in 2030, and there will be a greater intensity of heat islands than in 2020.

1. Introduction

Anthropogenic heat emissions are increasing as urbanization continues to rise, and issues with the urban ecological environment are getting worse. Urban construction causes the original vegetation and soil on the surface to be covered with impermeable surfaces such as cement and asphalt. These changes increase heat flux and reduce water vapor emission, resulting in a significant increase in urban temperature, known as the urban heat island effect [1, 2]. Environmental problems caused by urban heat island, such as the deterioration of air quality and the increase of extreme high temperatures [3], have seriously endangered people's production and living environment. Studies have shown that high temperatures weather is highly correlated with mortality from some diseases and mental health [4–6]. In order to enhance people's quality of life, it is crucial to develop urban land logically and reduce urban heat islands.

As one of the external characteristics of urban environment, the variation of urban surface temperature is positively correlated with the area of impervious surface [7, 8]. Land change is closely tied to environmental change since it impacts not just the natural environment that humans depend on for living, such as the climate and vegetation, but also the earth's energy and material cycles [9]. Since the International Geosphere-Biosphere Pla-n(IGBP), and the International Human Dimensions Programme on Global Environmental Change(IHDP) jointly put forward the "land use/cover change" program in 1995, the land cover change has become one of the research hotspots in the world environmental field [10, 11].

At present, the models used to study land cover change mainly include cellular automata-Markov-Chain(CA-Markov) [12], conversion of land use and its effects at small regional extent(CLUE-S) [13], slope-land use-exclusion-urban extent-transportation-hill shade model(SLEUTH) [14], artificial neural network(ANN) [15], and agent-based model(ABM) [16]. Among them, the CLUE-S model is rarely coupled with other models, and the selection of driving factors for land use is limited by scholars' own knowledge reserves [17]. The SLEUTH model cannot identify the weight factors of land development and pay too much attention to some edge factors. It will lead to unreasonable memory allocation, and the simulation results will be quite different from the actual situation [18]. The ANN model cannot quantitatively evolve the land-use data, which will lead to a long simulation cycle and unguaranteed accuracy [19]. The ABM model is usually used for local small-scale land-use simulations such as a school or a farm, not for urban areas [20]. Cellular automata (CA) in CA-Markov model can simulate its dynamic change in complex spatial form, and the Markov model is sensitive to temporal form. The combination of the two can improve the accuracy of land-use prediction [21–24], so there are many research precedents at home and abroad. CA-Markov model can predict land expansion on the urban scale well [25] and can also analyze the influence of different factors such as road and slope on urban expansion [26]. Using CA-Markov simulation to predict land use type and then retrieve the land surface temperature, so that urban heat island intensity can be analyzed [27].

The composition of underlying surface has significant influence on the intensity of urban heat island [28]. And how to qualitatively analyze the urban thermal environment according to the land use situation is also the key to research. The coupled Weather Research & Forecasting (WRF) model has different physical processes to describe various complex climate phenomena and has been widely used in meteorological research in recent years [29], including Andalusia, Spain [30], Portugal [31], Japan [32], New York, USA [33], and so on. However, the underlying surface data used by WRF is the United States Geological Survey (USGS) land-use data released by the US Bureau of Investigation in 1993, which includes 24 types of land-use. The second is Modis land use data of 20 land-use types updated in 2001 [34]. There are some differences between the two kinds of land use data and the actual land use data. Therefore, scholars at home and abroad have carried out some research on how to improve the accuracy of WRF meteorological simulation. Using CA-Markov model to generate land use data, Chen verified the applicability of land use data obtained by this method to simulate urban thermal environment in WRF [35]. And by coupling refined land use data in Chengdu with a single-layer urban canopy model, Xiao proved that higher resolution underlying surface data can improve the accuracy of WRF weather prediction [36]. In order to predict the distribution of urban thermal environment under different urban development scenarios, Li and Mochida adopted CA-Markov model to predict urban expansion and replaced land use data in WRF [37].

On the basis of previous research, this study sums up the experience. After predicting the spatiotemporal change of the self-classified land use data, it is coupled with the meteorological model. It not only improves the simulation accuracy of the study, but also shows how changing land use data affects urban heat islands over time. By predicting land surface temperature directly, this study streamlines the urban heat island calculation procedure and offers a more visual way to examine the relationship between land use and urban heat island across time.

This paper used remote sensing technology to extract high-precision land use data and used the CA-Markov model to build a land use data simulation and prediction scheme. Then, the simulated land use vector data was input into the WRF to simulate the urban heat island effect in the main urban area of Wuhan, and the temperature field and wind field data of Wuhan in July 2020 were obtained. By comparing with the observation data from weather stations, the feasibility of this method was verified in the study of the effect of urban heat island. Finally, the weather of Wuhan City in 2030 was predicted, which provided a new reference for rational planning of urban construction and the construction of urban ecological environments in the future.

2. Study Area

Wuhan is located in the central plain area and has a subtropical monsoon climate. It is located between 113°41E~115°05′E and 29°58N~31°22′N. With abundant rainfall throughout the year and hot temperature in summer, the highest temperature can reach nearly 40°C, Wuhan is known as China's furnace city [38]. The main urban area of Wuhan city is selected as the simulation area for the study. The main urban area (Figure 1) can be viewed as a microcosm of the rapid development of the city's explosive recent expansion. With rapid economic growth, the city area is gradually expanding (Figure 2) and the phenomenon of urban heat island is getting worse [39].

3. Research Method

3.1. Acquisition of Remote Sensing Data. The Landsat-5 ME (Thematic Mapper) dataset and the Landsat-8 OLI (Operational Land Imager) dataset were selected for the remote sensing data. To avoid cloudiness interference, the cloudiness of the selected remote sensing data was less than 5%.

The remote sensing images obtained were reclassified in Arcgis. Based on a land use classification system for remote sensing data developed by USGS in 1976 [40], the land-use status of Wuhan was divided into six categories: building land, farmland, forest, bare land, lake, and river. High-precision Landsat land use data were able to be acquired in this manner.

3.2. CA-Markov Model. A Markov chain is a process of randomly switching from one state to another in the state space. This process requires "memoryless," which means that the morphological distribution of the next state has nothing to do with the past state but is only determined by

Figure 1: Research area: the main urban area of Wuhan city (point 1 is the urban weather station, points 2 and 3 are the suburban weather station).

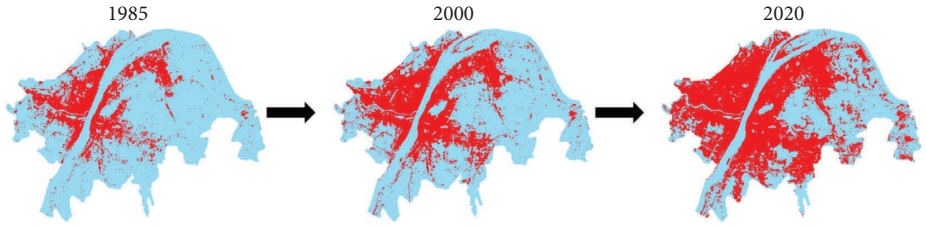

Figure 2: Changes throughout time in the built-up area of the main urban area of Wuhan (the red area represents the built-up area).

the current state [41]. In LUCC (land use and land cover change), this model can be used to describe the probability of conversion between different land classes [42]. For this, the specific formula of the Markov model is as follows:

$$S_{t+1} = P_{ij} \times S_t, \tag{1}$$

$$P_{\mathrm{ij}} = \begin{bmatrix} P_{11} & P_{12} & \cdots & P_{1n} \\ P_{21} & P_{22} & \cdots & P_{2n} \\ \vdots & \vdots & \vdots & \vdots \\ P_{n1} & P_{n2} & \cdots & P_{nn} \end{bmatrix}. \tag{2}$$

In the formula, S_{t+1} and S_t refer to the land-use type data of the area studied area at different times. P_{ij} refers to the probability transfer matrix under specific conditions.

The cellular automata (CA) model is a grid dynamic model with discrete time, space and state, and spatial interaction and temporal causality all being local [43]. The formula is as follows:

$$S_{t+1} = f\left(S_t, N\right). \tag{3}$$

In the formula, S_t refers to the land-use type at t time. N refers to the neighborhood interval of the target point. f represents the land use type transfer rule within the domain interval.

The CA-Markov model combines both two models to make the land types change not only with time according to specific laws but also show the change in space directly. The CA-Markov model makes it possible to change land use types in multiple and dynamic ways and is widely used in LUCC simulation research.

3.3. WRF Model. The research relied on WRF for simulation and adopted a nested grid design. Taking the latitude and longitude (114.30E, 30.50N) of the center of the main urban area as the simulation center, three layers of nesting were set successively (Table 1). Nesting of the third layer was the main research content.

Table 2 shows the initial weather boundaries required for WRF operation, with the FNL data used for simulation in 2020 and the CMIP6 data used for both the simulation in 2020 and the future simulation in 2030. For the future (2030) simulation, SSP245 scenario has been used. Based on the rate of greenhouse gas emissions, the SSP is a list of five possible development scenarios envisaged by the Intergovernmental Panel on Climate Change (IPCC) [44]. Among these, SSP2 is a medium development path that follows the historical development scenario, with no significant change in economic development and a slow decline in CO_2 emissions.

3.4. Verification of Simulation. The mean error (ME), the root mean square error (RMSE), and the consistency index (d) were used to qualitatively evaluate the simulation. The formula for calculating the mean error is as follows:

$$\mathrm{ME} = \frac{1}{n}\sum_{i=1}^{n} |P_i - O_i|. \tag{4}$$

Here, P_i is the predicted value, and O_i is the observed value. ME is an estimate of the reliability of the simulated data. When the value of ME is small, the reliability of the simulation is good. In contrast, the simulation is not so reliable.

The smaller the value of RMSE, the closer the simulated value is to the measured value, the better the simulation effect. The formula to calculate RMSE is as follows:

$$\mathrm{RMSE} = \sqrt{\frac{1}{n}\sum_{i=1}^{n} (P_i - O_i)^2}. \tag{5}$$

Here, P_i is the predicted value and O_i is the observed value.

The range of values of the consistency index is [0, 1]. The larger the value, the smaller the deviation from the measured value. When the value of d is 1, the simulation is completely consistent with the measured value [45, 46]. The formula for calculating d is as follows:

$$d = 1 - \frac{\sum_{i=1}^{n} (P_i - O_i)^2}{\sum_{i=1}^{n} \left(|\overline{P_i}| - |\overline{O_i}| \right)^2}, \tag{6}$$

In this formula, $\overline{P_i} = P_i - \overline{P}, \overline{O_i} = O_i - \overline{O}, \overline{P}$ is the average of the predicted values, and $\overline{O}$ is the average of the observed values.

3.5. Simulation Process. The flow chart of this study is shown in Figure 3. The first step was to divide the land-use data of the main urban area of Wuhan into six categories in 2007, 2013 and 2020. The above three images were input into IDRISI software and the CA-Markov model was used to realize land use transfer in the main urban area of Wuhan. The land use transfer matrix for 2007–2013 was produced via Markov operation after the land use data for 2013 and 2007 were used as a baseline. Based on the 2013 land classification data, the CA-Markov operation was carried out using the 2007–2013 land use transfer matrix to simulate the 2020 land use data. Similarly, land use data for 2030 can be predicted based on Landsat land classification data for 2013 and 2020.

The second step was the simulation and prediction of meteorological data, which was carried out through the WRF. The land-use data set provided by WRF is based on the 2001 resolution remote sensing image product MODIS [47]. In Landsat-2020, the MODIS data were replaced with the real 2020 land cover data. In CA-Markov-2020, the MODIS

Table 1: Nesting region in WRF simulation.

	D01	D02	D03
Grid size (km)	5.00	1.67	0.56
Number of grids	49×49	73×73	85×73
Vertical levels		34	

Table 2: Boundary conditions used as preprocessing in WRF simulation.

	CMIP6	FNL
Spatial accuracy	1.25°	1°
Time	6 h	6 h
Variables	Air temperature, wind speed, sea surface temperature, sea surface pressure, surface pressure, relative humidity, soil moisture, soil temperature, geopotential height	

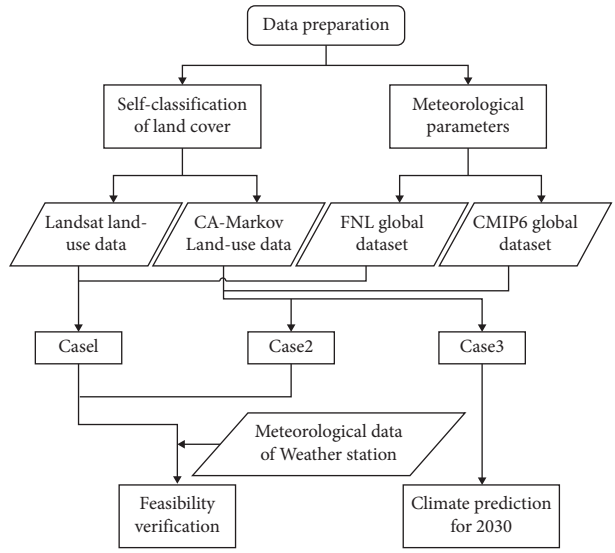

Figure 3: Study flowchart.

Table 3: Working condition setting in WRF simulation.

Case	1 (landsat-2020)	2 (CA-Markov-2020)	3 (CA-Markov-2030)
Simulation period	2020.06.30, 0:00~2020.08.01, 0:00(GMT)		2030.06.30, 0:00~2030.08.01, 0:00(GMT)
Geo scheme	Landsat	CA-Markov	CA-Markov
Meteorological parameters	FNL	CMIP6	CMIP6
Physics options	Parameter scheme		
Microphysics models	WSM 3-class scheme		
Longwave radiation scheme	RRTM scheme		
Shortwave radiation scheme	Dudhia scheme		
Surface layer models	Monin-Obukhov similarity theory		
Land surface models	Noah land surface model		
Planetary boundary layer	Mellor-Yamada-Janjic scheme		

data were substituted by the simulated 2020 land cover data. The WRF was used to calculate the climate parameters in 2020, to explore the impact of changes in land use data on urban heat islands and predict future climate conditions in 2030. The specific working conditions are set in Table 3.

Verifying and analyzing the simulation findings was the third step. Simulated land use data in 2020 was compared with self-classified land use data in 2020 to verify the prediction accuracy of the CA-Markov model. The simulated climate parameters were compared with the weather station data to verify the feasibility of the research method. To forecast and analyze future climate conditions, the forecast findings for 2020 and 2030 were compared.

4. Analysis and Discussion

4.1. Validation of the Land Cover Model. Based on self-classified land cover data from 2007 to 2013, the CA-Markov model was used to simulate the land cover scenario of 2020. After then, the accuracy of the CA-Markov model was confirmed by comparing it with the actual land cover in 2020.

4.1.1. Change in Self-Classified Land Cover from 2007 to 2020. The land use Status Map Classified by Landsat is shown in Figure 4. From 2007 to 2020, the extent of forests, lakes, and rivers has been most preserved, with little change in area (Table 4). Due to the city's explosive growth, the amount of agriculture fell by 132.7 km^2 between 2007 and 2013, and its share dropped quickly from 47% to 34%. From 2007 to 2020, the area of building land increased by 149.12 km^2 in total, with the main construction area concentrated in the southeast, and the built area of Hanyang District increased significantly from 2017 to 2013. By 2020, the area of the building land represented the largest proportion, most of which was transformed from farmland. A tiny portion of the forest was turned into farmland, and the area of bare land, lakes, and rivers changed negligible.

4.1.2. Comparison between Simulated and Measured Land Use Type. Figure 5 shows the land use classification image for 2020 simulated by the CA-Markov model. The 2020 simulated land use data was compared with Landsat classified data to verify the accuracy of the model (Table 5). The relative errors of farmland, building land, and lakes were all less than 3%. The simulated area of bare land differed from the measured area by 4.32 km^2, but the proportion of bare land was less than 1%, so the error is negligible. The area of lakes simulated by CA-Markov was 24.87 km^2 less than that of the actual, and the forest area was 11.86 km^2 more than that of the actual. Compared with the actual area, these two types of land area deviation are large, but their respective proportions are less than 10%. In general, the simulated area of the six land classes is approximately the same as the actual classified area, and the two sets of data have significant correlation.

The Kappa coefficient, whose value range is [0, 1], which was computed by the Crosstab module in IDRISI, was used to confirm the prediction accuracy of the overall land type distribution in 2020. When the Kappa coefficient is greater than 0.75, it proves that the consistency of the two images is high [48]. The calculated Kappa coefficient is 0.8217, which proves that the prediction accuracy of CA-Markov is high (accuracy validation of the land cover data.).

4.2. Comparison of Measured Climate and Predicted Climate of the WRF Model. The simulations' accuracy was confirmed by comparing the parameters for wind velocity (10 m) and high temperature (2 m).

4.2.1. Temperature Verification at 2 m. To verify the accuracy of the simulation, the weather station data was compared with the simulated values. Both simulations (Figures 6 and 7) accurately replicate the temperature fluctuation trend at 2 m, and the simulated values of CA-Markov-2020 are slightly higher than the observed values. Wuhan had a lot of rainy days in July 2020. The simulation effect of the two simulations was better on bright days such as the ninth and 22nd, while there were some differences in the simulation of extreme rainy days such as 3–5.

The average error of Landsat-2020 was the smallest among the three weather stations, but both two simulations could show the trend of the daily temperature change. The simulation of both conditions is very good (Table 6).

The value of d in Landsat-2020 is higher than that of CA-Markov-2020, indicating that the simulated value of Landsat-2020 is the closest to the measured value. The RMSE values of the two simulations are somewhat large, and the

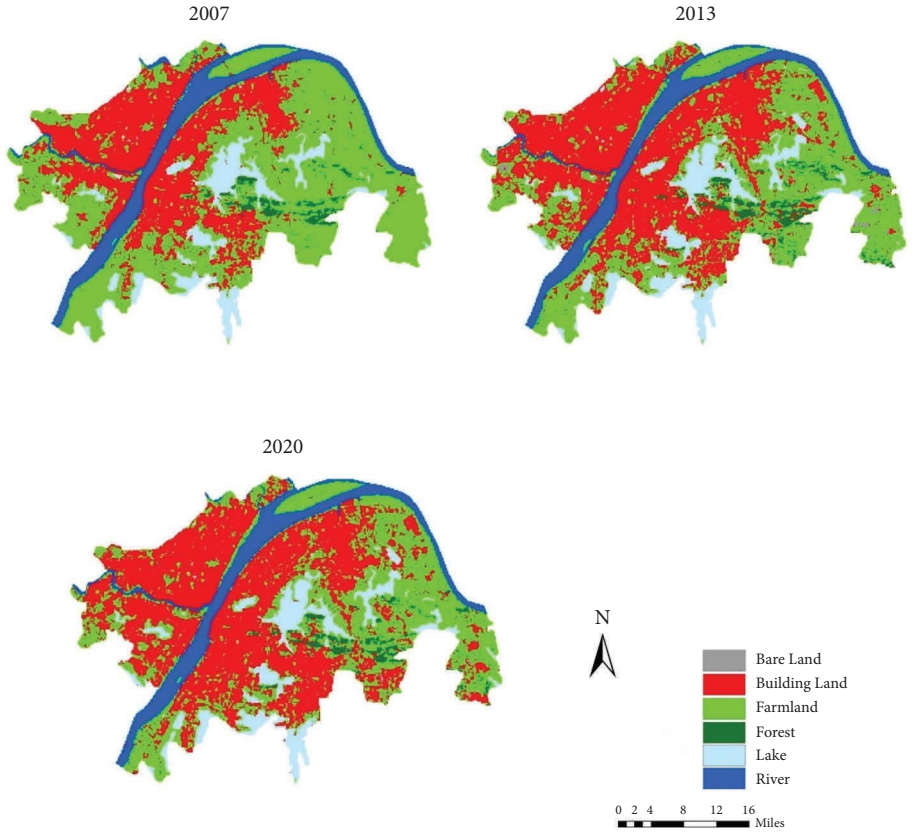

Figure 4: Classification of land-use status from 2007 to 2020.

Table 4: Proportion of land-use types from 2007 to 2020.

Year/proportion of land types	2007		2013		2020	
	km^2	%	km^2	%	km^2	%
Farmland	473.11	47.29	340.41	34.04	318.42	31.81
Building land	310.12	31.00	422.58	42.26	459.24	45.88
Forest	21.58	2.16	31.11	3.11	21.17	2.11
Bare land	2.82	0.28	9.14	0.91	3.97	0.40
Lake	89.81	8.98	99.66	9.97	95.14	9.51
River	102.93	10.29	97.12	9.71	102.97	10.29

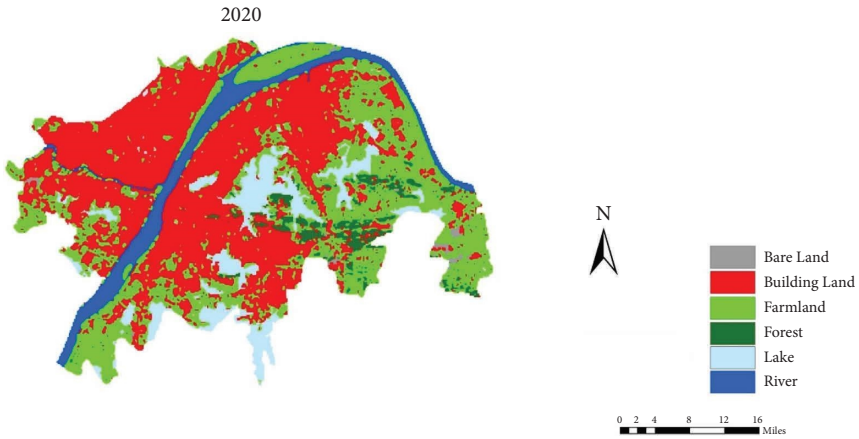

Figure 5: Simulated land-use image for 2020.

Table 5: Error analysis of the proportion of land use types in 2020.

Proportion of land types	Landsat		CA-Markov		RE (%)	R^2
	km^2	%	km^2	%		
Farmland	318.42	31.81	308.65	30.97	3%	0.997
Building land	459.24	45.88	474.85	47.64	3%	
Forest	21.17	2.11	33.03	3.31	36%	
Bare land	3.97	0.40	8.29	0.83	52%	
Lake	95.14	9.51	93.84	9.41	1%	
River	102.97	10.29	78.10	7.84	32%	

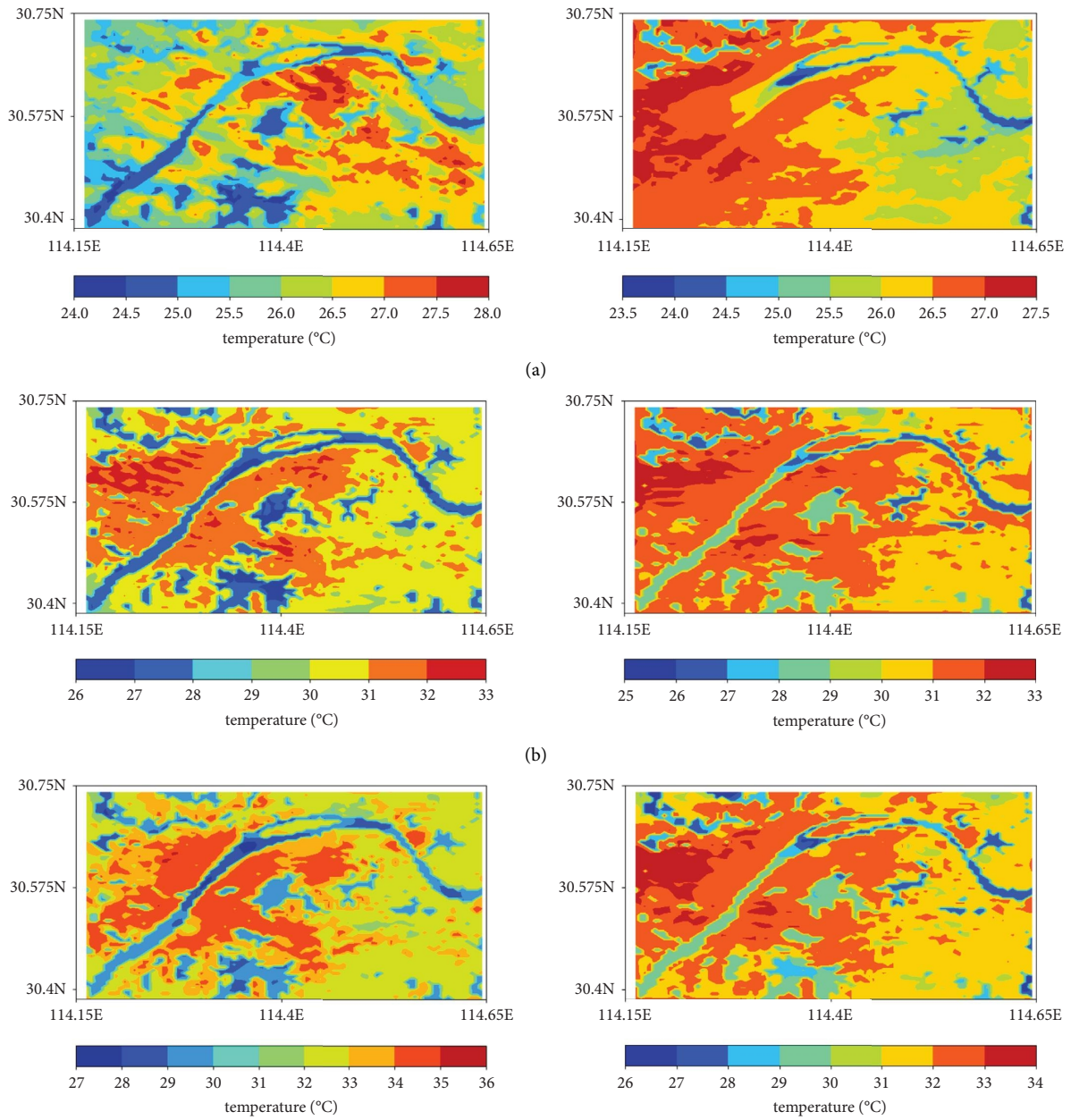

Figure 6: Continued.

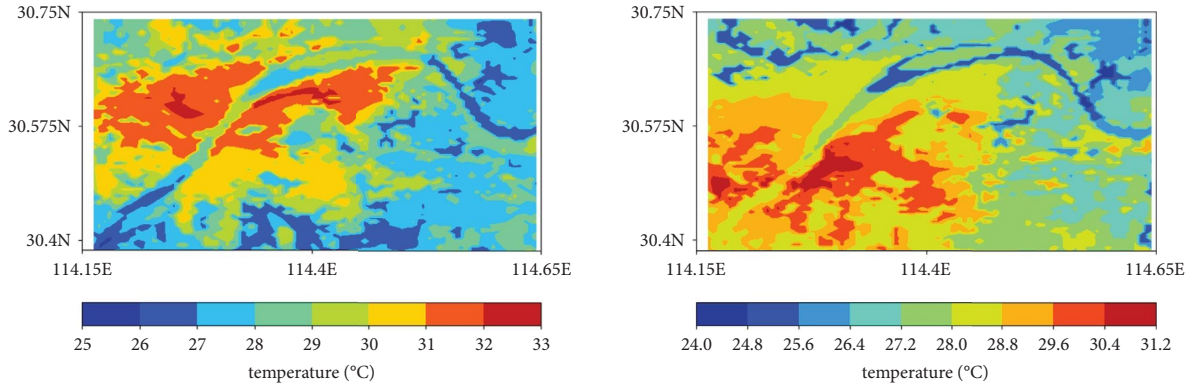

(d)

Figure 6: Temperature cloud images of the main urban area of Wuhan on 9 July 2020 (the left side is landsat-2020 and the right side is CA-Markov-2020). (a) 8:00, (b) 12:00, (c) 16:00, and (d) 20:00.

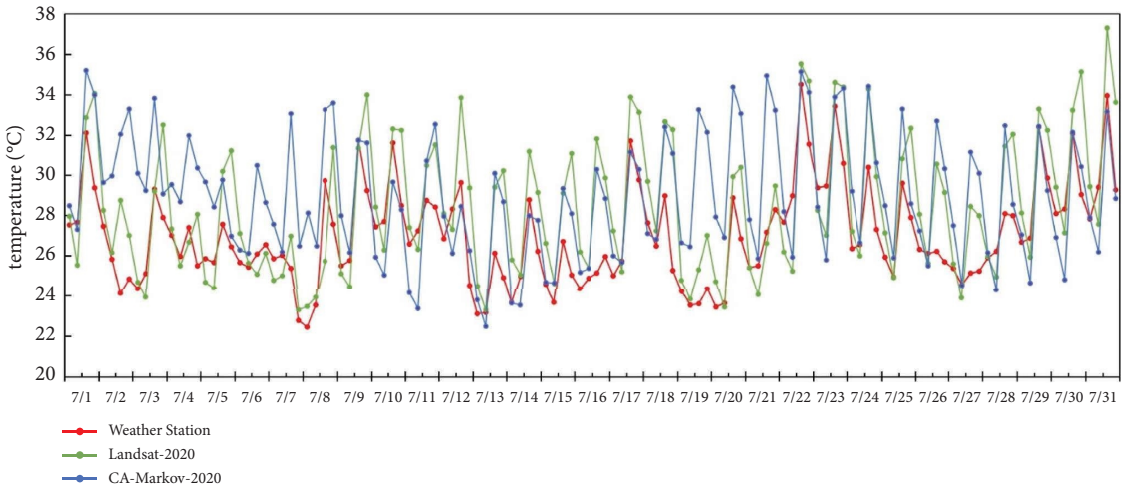

(a)

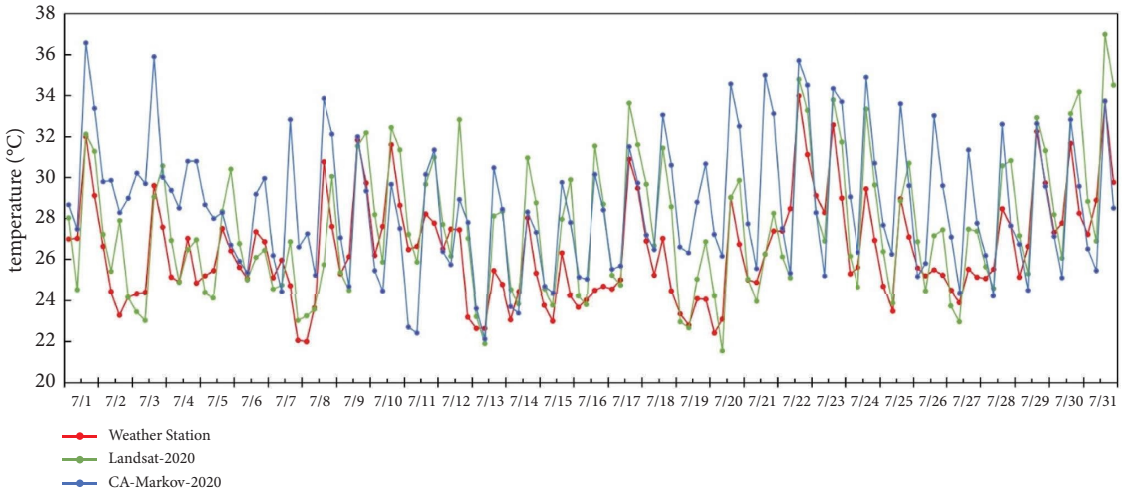

(b)

Figure 7: Continued.

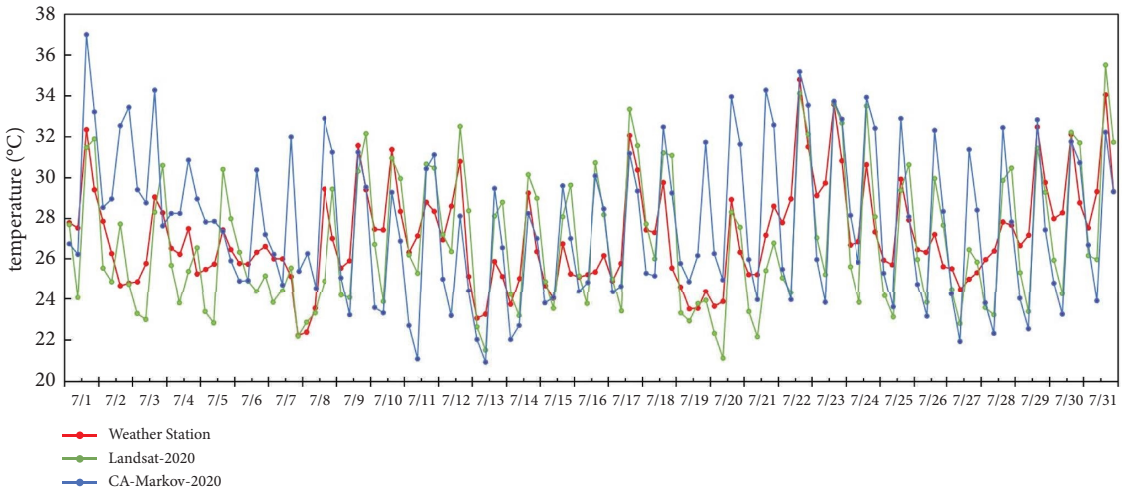

(c)

Figure 7: Temperature at 2 m of each weather station in the main urban area of Wuhan in July 2020. (a) Point 1. (b) Point 2. (c) Point 3.

Table 6: Error analysis of temperature at 2 m.

		Point 1	Point 2	Point 3
ME	Landsat-2020	1.90	1.62	1.56
	CA-Markov-2020	2.72	2.89	2.55
d	Landsat-2020	0.81	0.86	0.88
	CA-Markov-2020	0.75	0.74	0.74
RMSE	Landsat-2020	2.49	2.13	1.93
	CA-Markov-2020	3.50	3.58	3.56

simulation effect of the suburban weather station is superior than that of the urban weather station. The simulation effect of the temperature at 2 m in Landsat-2020 is good. The *d* value and the RMSE value of CA-Markov-2020 are larger than those of Landsat-2020. However, considering the uncertainty of future land change and climate change, the error of CA-Markov-2020 is considered to be within an acceptable range. That is, the CA-Markov condition has certain applicability in temperature simulation.

Combined with the specific weather and temperature analysis, the temperature field is analyzed on July 9 at 8:00, 12:00, 16:00, and 20:00 as it is a sunny day (Figure 6). At eight o'clock, all other areas had temperatures that were concentrated at roughly 25°C on the Landsat-2020 simulation except for the built-up area. With the exception of the water, which was 24°C, the rest of the CA-Markov-2020 simulation had a rather high total temperature of 28°C. Similarly to the land use image, the high temperature area of the two simulated simulations was concentrated in the built-up area and the low temperature area was concentrated in the water. At noontime, due to solar radiation, the temperature in most areas of both simulations rose to 32°C. Due to the high specific heat capacity of water, the temperature of lakes and rivers rises slowly, and the temperature is maintained at 26°C.

The difference in the temperature distribution of the two simulations at six o'clock at night was similar, and the high temperature area was roughly the same, concentrated in the building land, and the maximum temperature could reach 35°C. Farmland and forests made up the sub-high temperature zone, which was roughly 3°C cooler than the high temperature zone. The area with the lowest temperature was the lakes and rivers, where the temperature was around 28°C. The temperature of CA-Markov-2020 is somewhat greater than that of Landsat-2020, which can be attributed to the overestimation of future temperature by CMIP6 dataset [49]. The average temperature of CA-Markov-2020 at 8 pm was 2°C lower than that of Landsat-2020, but the high temperature region was still in the built-up area and the temperature of other land types was concentrated at 25-26°C. The Landsat-2020 temperature distribution showed a more pronounced disparity. The highest temperature on the building ground was 33°C and the temperature in the rivers and lakes was 27°C. The temperature of water fluctuated slowly with the temperature of air, so the temperature basically remained unchanged. It is evident from both examples that the heat island region of Wuhan's main urban area is centered on the eastern and central banks of the Hanjiang River, which is in line with the area's general development tendency [50]. The analysis above demonstrates the suitability of the CA-Markov condition for temperature modeling.

4.2.2. Wind Velocity Verification at 10 m. Wuhan City's wind speed in July 2020 is depicted in Figure 8. The diurnal variation trends of the two models at the three weather stations were somewhat overestimated, but they were compatible with the real results. On the 7th and 22nd, the actual wind velocity was high, and the simulation effect of the two simulations was excellent at this time. It demonstrates that at high wind velocities, Landsat-2020 and CA-Markov-2020 have the best simulation effect. When the actual wind speed was low, Landsat-2020 was more in line with the observed values. Landsat-2020's wind velocity was 1.1 m/s higher than the average recorded value, and the wind velocity of CA-Markov-2020 was 2.18 m/s higher (Table 7).

While the Landsat-2020 simulation effect was better and more consistent with the measured values, the agreement coefficients of the two simulations at the three weather stations were relatively low. The RMSE of CA-Markov-2020 was larger than that of Landsat-2020, but both errors were within the allowable bounds. It is proven that there is a certain deviation between simulation and measurement in the simulation of wind velocity at 10 m. The simulation effect is better when land use data is replaced by high-precision land use data, while CA-Markov simulated land use data can also be used to simulate an urban wind environment.

4.2.3. Analysis of the Heat Island in 2020. The intensity of the urban heat island in the main urban area of Wuhan in July is shown in Figure 9. For Point 2, the mean heat island intensity of the weather station was 0.63°C. The highest recorded temperature of 2.1°C was recorded at 23:00 on July 3. It can be seen that the intensity of the urban heat island intensity is strong at night and weak at midday from the fluctuation of heat island intensity observed by weather stations. The average intensity of Landsat-2020 heat island was 0.93°C, and the maximum heat island recorded at 16:00 on July 18, which was 4.41°C. The negative heat island peaked on July 31 at 17:00, with a temperature of −1.71°C. The average heat island intensity of CA-Markov-2020 was 0.65°C and the peak heat island intensity was 6.66°C that occurred at 13:00 on July 19. The minimum negative heat island was −5.12°C, which recorded at 11:00 on July 3. The three curves' daily fluctuations were essentially consistent, and the degree of agreement was better on sunny days, such as the ninth. On the 3rd and 19th, the weather could vary in a single day. At this time, the simulation error of the two conditions was a little bit high.

The maximum heat island intensity of Point 3 was 1.14°C, and it was visible at midnight on July 9. The minimum intensity of the negative heat island was −1.98°C, which recorded at 13:00 on July 12. The intensity of the heat island observed by the weather stations did not fluctuate much, but the intensity of the negative heat island was large. Following 2008, the primary urban area's development land mostly evolved in a southeasterly direction [50], with the area surrounding Point 3 seeing a sharp growth in building land. The growth of the built-up region was accompanied by the reduction of water and forest, raising the temperature close to Point 3 and intensifying the negative heat island. The greatest intensity of the heat island simulated by Landsat-2020 was 4.9°C, which recorded at 17:00 on July 16, and the negative heat island situation basically did not appear. The maximum heat island intensity of CA-Markov-2020 was 8.43°C at 14:00 on July 19. On the 19th, the weather shifted from a rainy to a sunny day, and the weather change could not be replicated in the CMIP6 dataset, resulting in a high simulation temperature and a large simulation deviation of CA-Markov-2020. Compared to the observation data from the weather stations, the average heat island intensity simulated by Landsat-2020 and CA-Markov-2020 was approximately 1°C higher, indicating that the simulated temperature of Point 3 under the two conditions was too low. Due to urbanization, the actual temperature of Point 3 is higher, and the self-classified land use data could not well reflect the short-term rapid development, resulting in low simulated temperature.

4.3. Analysis of the Forecast Results for 2030

4.3.1. Change in Land Cover. The predicted land use statistics for 2030 are shown in Figure 10. Compared to 2020, the area of bare land, lakes, and rivers in 2030 has essentially not altered (Table 8). There will be a 6.81 km^2 drop in the forest and a 32.32 km^2 decrease in the farmland area. And the proportion of farmland will decrease to 28.7%, majority of which will be converted into building land. Under the urbanization process, construction land will account for 49.75% in 2030, which is more concentrated and encompasses a bigger area than it did in 2020.

4.3.2. Climatic Simulations. Land use data predicted by CA-Markov in 2030 and meteorological data from the CMIP6 dataset were used to simulate the future climate in 2030 (CA-Markov-2030). Since WRF has a great simulation impact for high-temperature weather, so the simulation results from 5 July were extracted to analyze the temperature distribution in the main urban area (Figure 11).

The temperature in most areas is about 27.5°C at 8:00. Built-up areas have substantial heat storage potential due to their dense building stock, which results in frequently higher temperatures. From the figure, it can be seen that the temperature in the place where the building land is concentrated is 1°C higher than other areas, and the temperature of water is the lowest. At noon, the sun is at its strongest. Except that the temperature of rivers and lakes is maintained at 29°C, the temperature in the rest of the area is above 33°C, with certain locations even reaching 36°C. The temperature at 16:00 is the same as it was at noon; the temperature of the water is maintained at 29°C, and the temperature in other areas is still around 35°C. At 20:00, the heat island zoning is clearly visible, and the temperature in the built-up area is obviously 4-5°C higher than that in other areas.

The intensity of the heat island in July 2030 is shown in Figure 12. For Point 2, the peak heat island intensity in July 2030 is 4.2°C, which occurs at 21:00 on 7th. The average heat island intensity is 0.73°C in 2030, which is stronger than in 2020. Point 3's greatest heat island intensity was 8°C, and it happened on July 21 at 18:00. The average heat island intensity is 1.43°C and the overall heat island intensity is higher than Point 2. The heat island intensities of the two weather stations are similar on the 14th. On the 14th, there is a high temperature and little wind. Given that the weather is likely to be bright, warm, and partly cloudy, so the heat island intensities of the two weather stations are similar. The heat island intensity on July 7 varies significantly between the two weather stations, indicating a contrary trend. Compared to Point 3, there are more buildings around Point 2. As a result, the temperature of point 2 will be occasionally much higher than that of point 3, which is also the reason why point 2 is a positive heat island, while point 3 is a negative heat island.

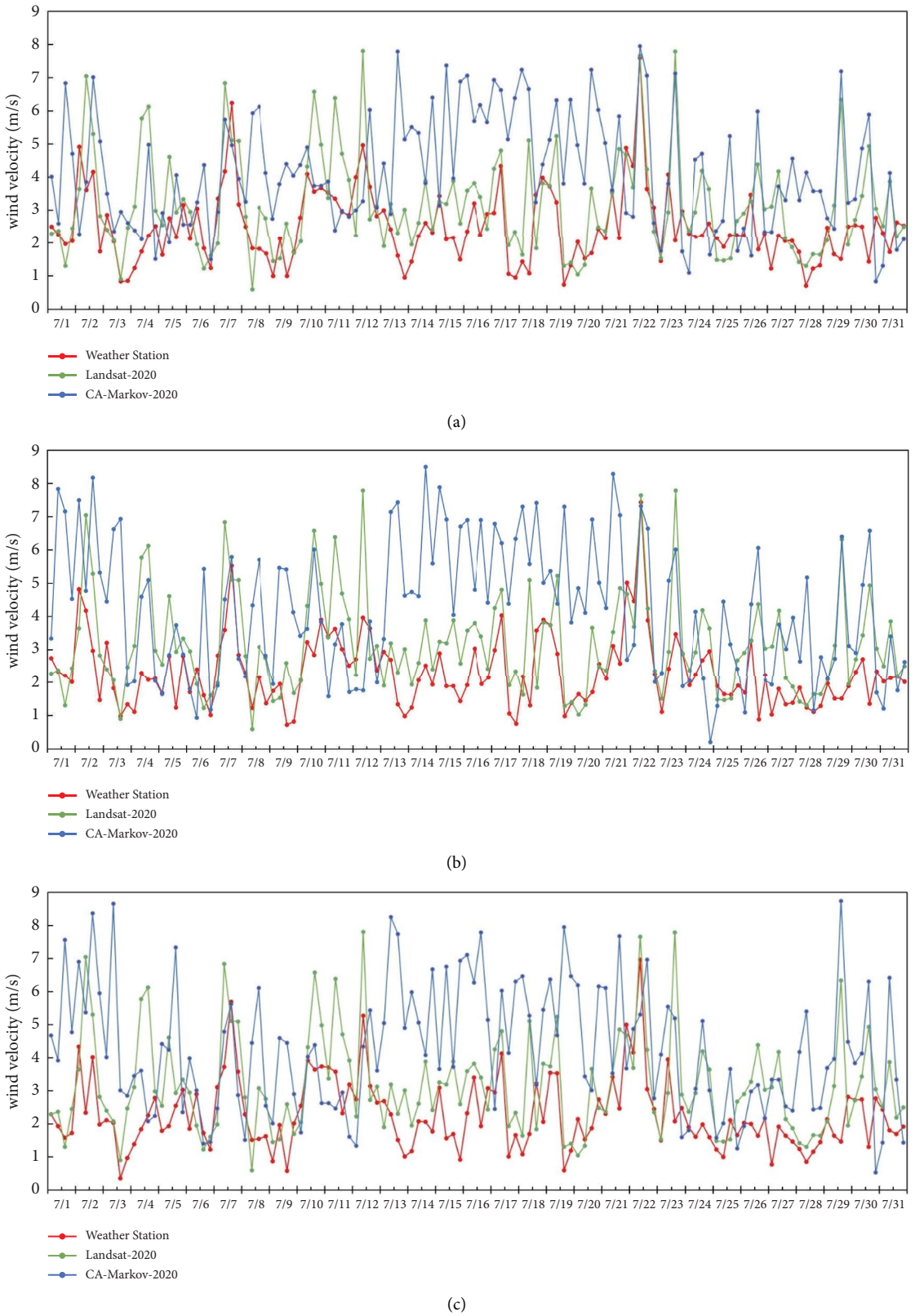

Figure 8: Wind velocity at 10 m of each weather station in the main urban area of Wuhan in July 2020. (a) Point 1. (b) Point 2. (c) Point 3.

Table 7: Error analysis of wind velocity at 10 m.

		Point 1	Point 2	Point 3
ME	Landsat-2020	1.07	1.12	1.11
	CA-Markov-2020	2.09	2.20	2.25
d	Landsat-2020	0.65	0.62	0.62
	CA-Markov-2020	0.43	0.40	0.36
RMSE	Landsat-2020	1.46	1.49	1.50
	CA-Markov-2020	2.66	2.78	2.80

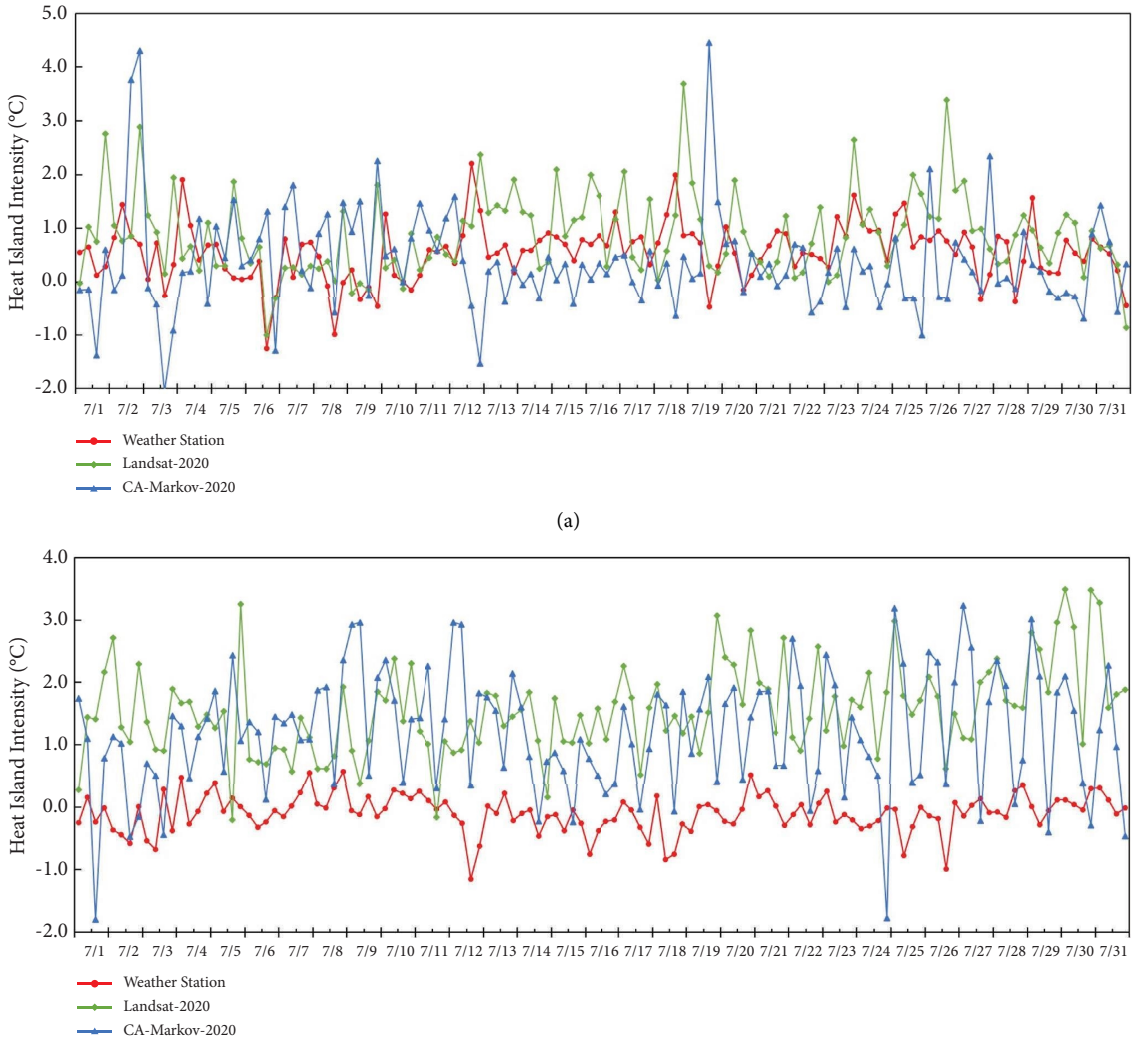

Figure 9: Changes in urban heat island intensity in the main urban area of Wuhan in July 2020 (UHI = $t_{urban} - t_{suburban}$). (a) Point 1-point 2. (b) Point 1-point 3.

The temperature at 2 m and the wind velocity at 10 m at three weather stations in 2030 were compared to those in 2020 (Figures 13 and 14). The daily temperature fluctuations simulated by the three weather stations are the same, with the highest temperature recorded at 14:00 on July 2. The average temperature of the urban weather station (Point 1) is 33.02°C, a maximum temperature of 41.88°C, and a minimum temperature of 24.95°C that occurs at 6 am on July 3. Between July 2 and 3, the temperature difference is large and the temperature difference at other periods is maintained at 6–8°C a day. Point 2 experiences an average temperature of 32.86°C, a maximum temperature of 42.49°C, and a minimum temperature of 22.48°C at 6 a.m. In 2030, the built-up area around Point 2 is larger in scope and therefore tends to be consistent with the temperature change of the urban weather station. The average temperature of point 3 is 31.97°C, the highest temperature is 41.21°C, and the lowest temperature is 22.47°C. Compared to the other two weather stations, the temperature is the lowest.

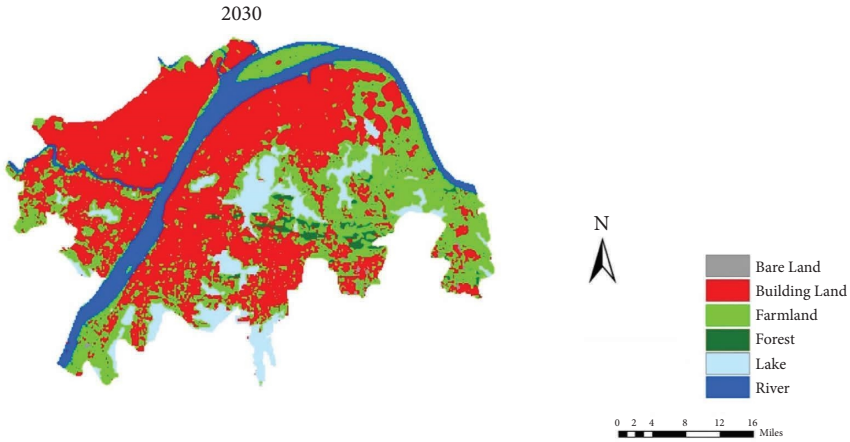

Figure 10: Classification of land-use status in 2030.

Table 8: Proportion of land-use types in 2030.

Year/proportion of land types	2020		2030	
	km^2	%	km^2	%
Farmland	318.42	31.81	286.11	28.70
Building land	459.24	45.88	496.00	49.75
Forest	21.17	2.11	14.36	1.44
Bare land	3.97	0.40	4.59	0.46
Lake	95.14	9.51	93.43	9.37
River	102.97	10.29	102.43	10.27

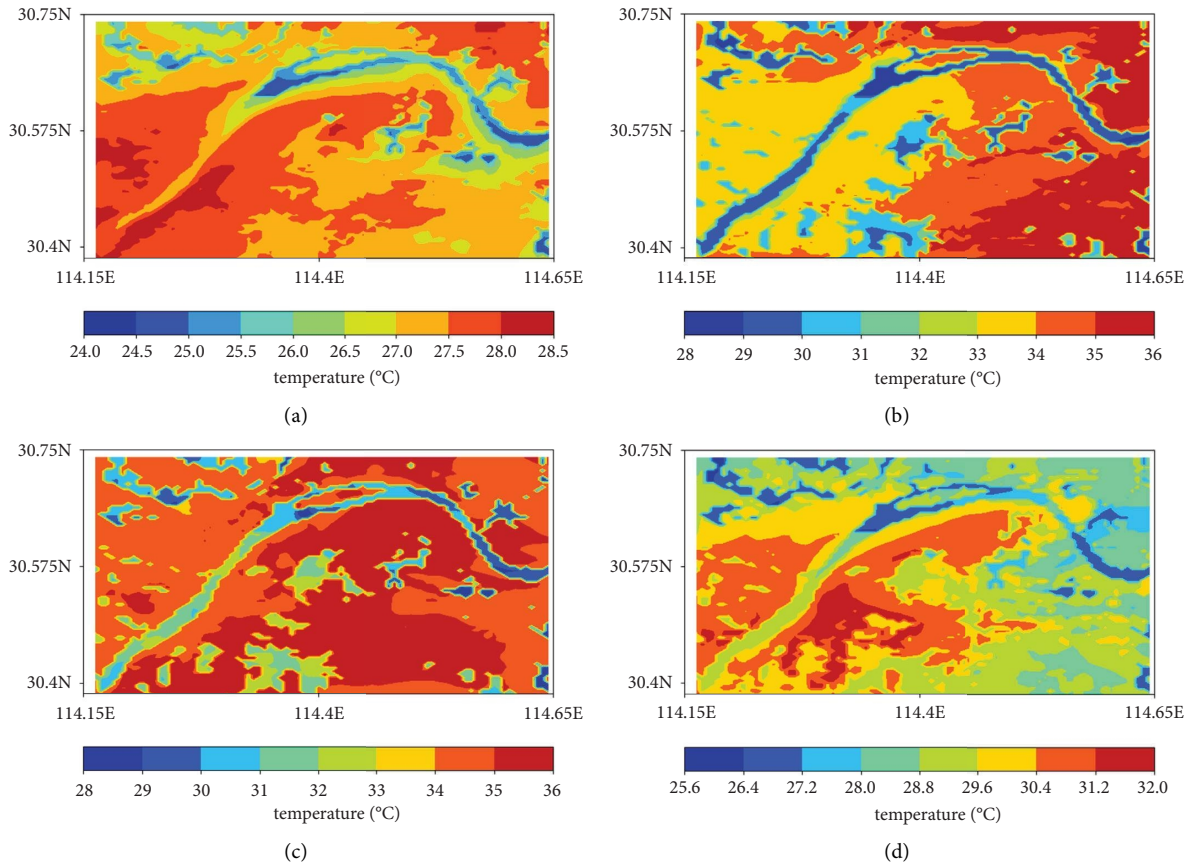

Figure 11: Temperature cloud image on July 5, 2030. (a) 8:00. (b) 12:00. (c) 16:00. (d) 20:00.

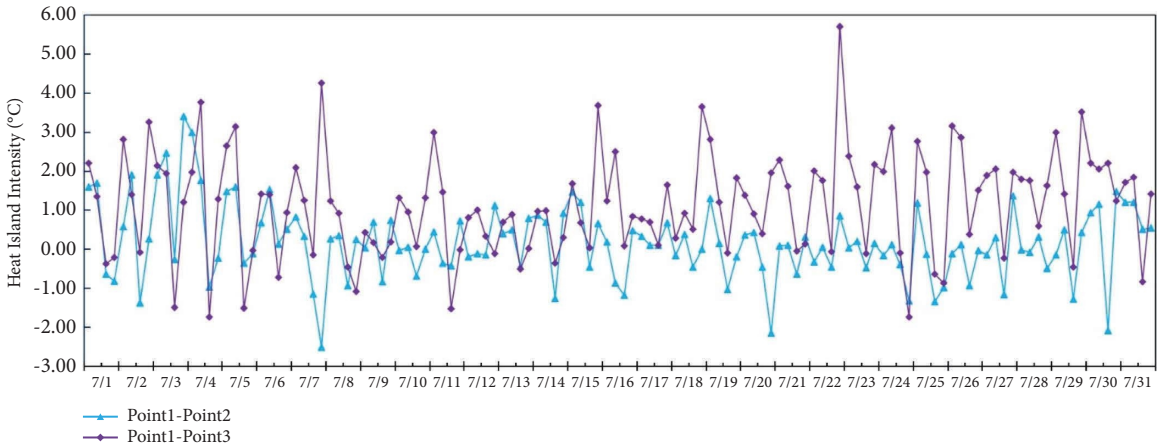

Figure 12: Urban heat island intensity in July 2030.

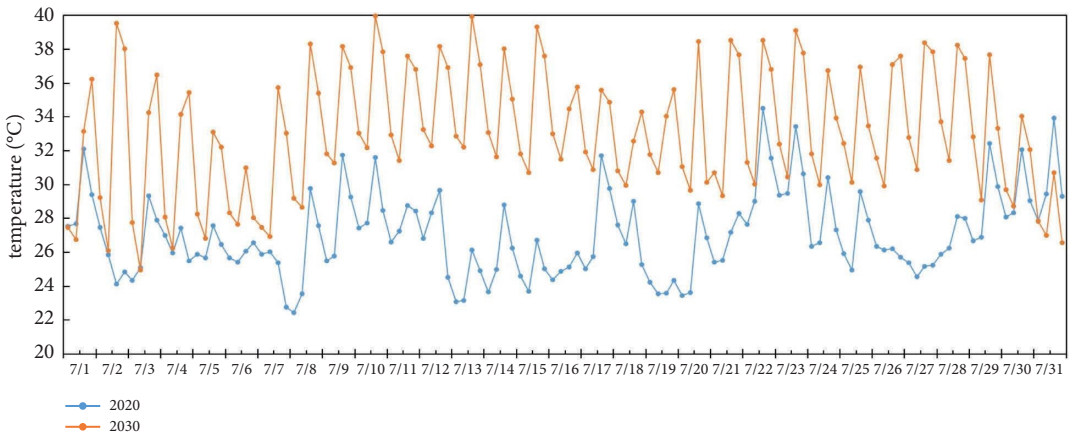

(a)

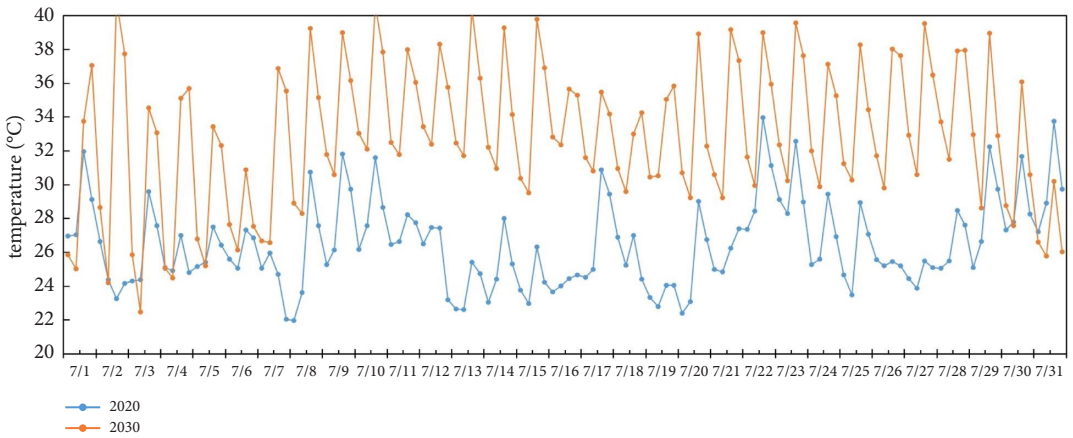

(b)

Figure 13: Continued.

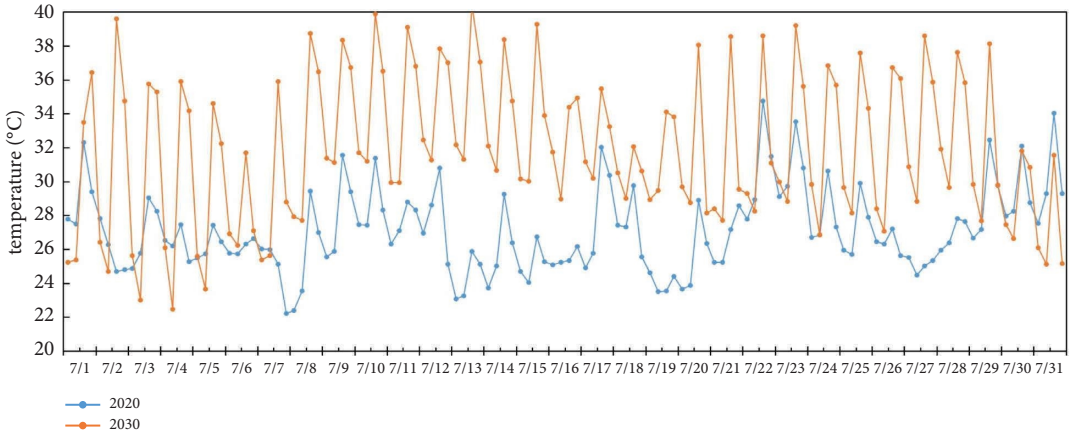

(c)

Figure 13: Comparison of temperature at 2 m in July 2030 and July 2020. (a) Point 1. (b) Point 2. (c) Point 3.

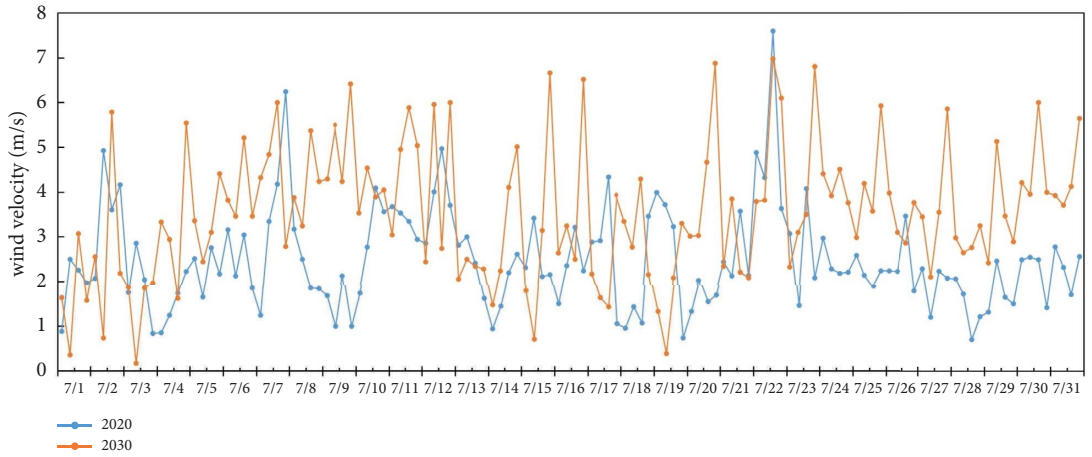

(a)

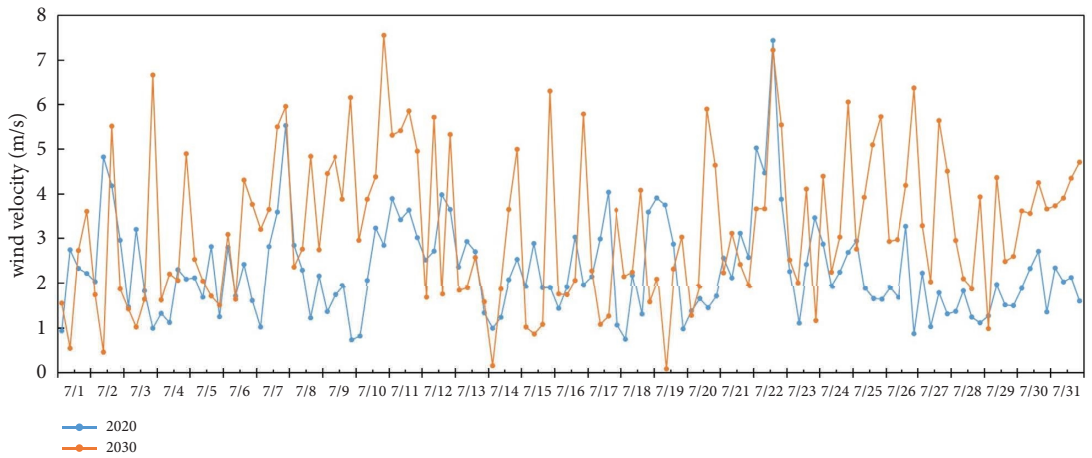

(b)

Figure 14: Continued.

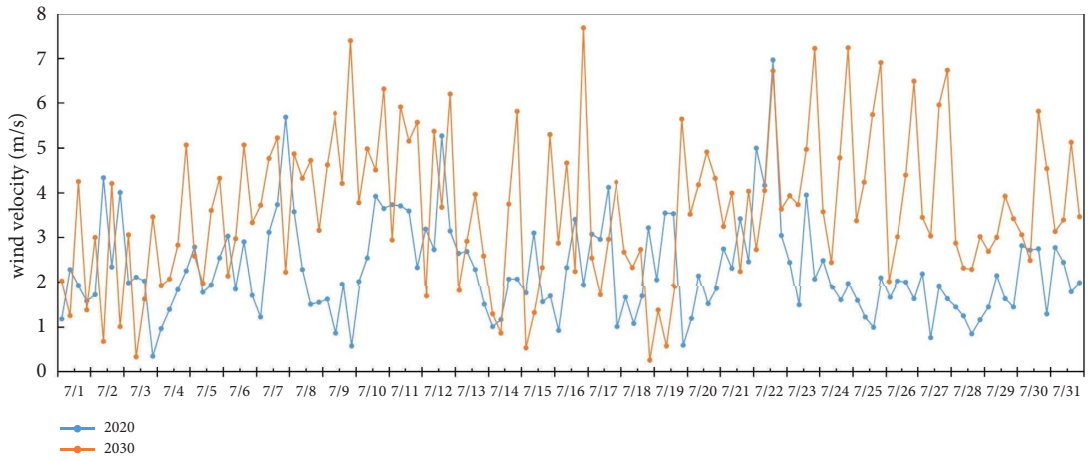

(c)

Figure 14: Comparison of wind velocity at 10 m in July 2030 and July 2020. (a) Point 1. (b) Point 2. (c) Point 3.

The temperature in 2030 is generally higher than that in 2020, with an average temperature increase of about 5°C. Point 2 has the most noticeable temperature increase, with an average increase of 6.3°C.

In 2030, the maximum wind velocity of Point 1 was 7.89 m/s, appearing at 9 a.m. on July 10, and the minimum wind velocity was 0.17 m/s at 5 a.m. on July 1. The average wind velocity at Point 1 is 3.53 m/s, and the maximum fluctuation of wind velocity can reach 5 m/s in a day, which has a large fluctuation. The average wind velocity at Point 2 is 3.22 m/s, and the maximum wind velocity is 7.77 m/s. Point 3 has an average wind speed of 3.56 m/s and a maximum wind speed of 7.89 m/s. Compared to the other two weather stations, Point 3 in 2030 is still located in a suburban area, so it has the lowest temperature and the highest wind velocity. The maximum wind velocity of three weather stations in 2020 is 7.66 m/s, which is marginally different from that in 2030. Nonetheless, the simulated average wind velocity in 2030 is 3 m/s, which is 1 m/s higher than that in 2020, indicating that the overall wind speed in 2030 has strengthened.

4.4. Discussion. It is found that the major urban region of Wuhan is expected to see a 32.32 km^2 drop in farmland area and a 36.76 km^2 rise in building land area by 2030. The temperature typically rises in tandem with an increase in built-up area. Based on the analysis of Landsat data in 2016 and 2021, Díaz-Chávez et al. discovered that the urban area of Columbia grew by roughly 3.13%. The yearly mean surface temperature rose by 0.68°C in five years as the built-up area increased [51]. According to Ezimand et al. simulation and prediction of the land use data of Rasht in 2031 using the CA-Markov model, the built-up area would grow to 102.9 km^2 in the future. It was discovered that there was a substantial positive correlation between the land surface temperature and the built-up area through temperature inversion [52].Surface temperatures can be directly calculated through the study. The urban heat island intensity of study area in 2030 rises to 0.73°C by calculating the temperature variation between urban and suburban areas.

It must be acknowledged that the study had some shortcomings. In this study, the refined land use data is only divided into 6 categories, there may be a concentration of building land in the process of CA-Markov, which could affect the simulation results. The research area is concentrated in the main urban area of Wuhan, and the scope is limited. In order to optimize the CA-Markov process and raise the accuracy of the simulation, the study scope may be increased in the future and land use data categorization can be more refined.

Even with its limitations, the study offers a fresh perspective on researching the climate of the future. By using land change scenario into research, the study can estimate future climate and provide a more logical way to predict the association between land cover change and urban heat island. The results are more intuitive and the process of calculating urban heat island intensity is less complicated when compared to temperature inversion [53, 54].

To prevent future deterioration of the urban environment, better protection of cold areas such as rivers and lakes [55, 56] should be an important consideration in the upcoming urban construction process. According to the existing development trend, the area of building land would grow in the future while the area of farmland would continue to decline. Reasonable planning can be carried out to spread out the built-up area and increase the green area, so that the mitigation effect of the cold area on the urban heat island can be brought into full play. And the coordinated development of economy and urban environment can be realized.

5. Conclusions

Using the CA-Markov model, this study simulated the land use data for 2020 and predicted the land use data for 2030. By substituting the WRF's underlying surface data, the main Wuhan urban area's climatic parameters for 2020 and 2030 were simulated. After an analysis of Wuhan City's urban heat island problem, the following conclusions were made.

(1) This study simulated land use data for 2020 using the CA Markov model, and errors in farmland, building land, and lake areas were all less than 3%. The distribution of the six simulated land types was roughly in the same way as the Landsat classification. With a Kappa coefficient of 0.82, the simulation accuracy is high.

(2) The average temperature error of the CA-Markov-2020 simulation was 2.5°C and the consistency index was about 0.75. The average error of the wind velocity was 2 m/s. In sunny, high-temperature conditions, the temperature division of the associated temperature field was clearly visible. The densely built-up area contained areas with high temperatures, whereas the water had the lowest temperature. CA-Markov model has good simulation effect on thermal environment simulation.

(3) The intensity of the urban heat island in 2020 ranged from −1 to 2°C. The daily fluctuation of urban heat island intensity simulated by Landsat-2020 and CA-Markov-2020 was the same as that measured. The overall fluctuation of the intensity of the heat island at Weather Station 2 was small, while at Weather Station 3, there were numerous instances of negative heat island conditions. The rapid development of the city caused vegetation and water near Weather Station 3 to decrease, which raised the temperature there.

(4) In July 2030, the average temperature would be about 5°C higher than in 2020, and the average wind velocity is 1 m/s higher. Weather Station 2 may become an urban weather station in the future building phase, as evidenced by the similarity in the extreme values and temperature variations between Weather Stations 1 and 2. In 2030, the scope of the built-up area is larger, the region is more concentrated, so the urban heat island phenomenon is obvious, and the intensity is also increased.

Data Availability

The weather station data used to verify the results of this study are available from the corresponding author upon request. The Landsat image data were downloaded from the website (https://earthexplorer.usgs.gov/). The FNL data were downloaded from NCAR website (https://rda.ucar.edu/datasets/ds083.2/index.html).

Conflicts of Interest

The authors declare that they have no conflicts of interest.

Acknowledgments

This work was supported by the National Natural Science Foundation of China (Grant nos. 51608405 and 51808410), the Hainan Province Science and Technology Special Fund (ZDKJ2021024).

References

[1] N. Yadav, K. Rajendra, A. Awasthi, C. Singh, and B. Bhushan, "Systematic exploration of heat wave impact on mortality and urban heat island: a review from 2000 to 2022," *Urban Climate*, vol. 51, 2023.

[2] H. Zhang, H. Q. Xu, L. Li, Y. Fan, and Y. P. Fan, "Analysis of the relationship between urban heat island effect and urban expansion in Chengdu," *China*, vol. 16, no. 1, pp. 70–78, 2014.

[3] K. Deilami, M. Kamruzzaman, and Y. Liu, "Urban heat island effect: a systematic review of spatio-temporal factors, data, methods, and mitigation measures," *International Journal of Applied Earth Observation and Geoinformation*, vol. 67, pp. 30–42, 2018.

[4] R. S. Kovats and S. Hajat, "Heat stress and public health: a critical review," *Annual Review of Public Health*, vol. 29, no. 1, pp. 41–55, 2008.

[5] W. Lee, M. L. Bell, A. Gasparrini et al., "Mortality burden of diurnal temperature range and its temporal changes: a multi-country study," *Environment International*, vol. 110, pp. 123–130, 2018.

[6] W.-H. Lee, Y. H. Lim, T. N. Dang et al., "An investigation on attributes of ambient temperature and diurnal temperature range on mortality in five east-asian countries," *Scientific Reports*, vol. 7, no. 1, 2017.

[7] N. A. S. Kasniza Jumari, A. N. Ahmed, Y. F. Huang et al., "Analysis of urban heat islands with landsat satellite images and GIS in Kuala Lumpur Metropolitan City," *Heliyon*, vol. 9, no. 8, 2023.

[8] J. Yan, C. Yin, Z. An et al., "The influence of urban form on land surface temperature: a comprehensive investigation from 2D urban land use and 3D buildings," *Land*, vol. 12, no. 9, p. 1802, 2023.

[9] J. Zhang, Z. Feng, and L. Jiang, "Progress on studies of land use/land cover classification systems," *Resources Science*, vol. 33, no. 6, pp. 1195–1203, 2011.

[10] J. Liu and X. Deng, "Progress of the research methodologies on the temporal and spatial process of LUCC," *Chinese Science Bulletin*, vol. 55, no. 14, pp. 1354–1362, 2010.

[11] Y. C. Tian and M. Z. Liang, "Quantitative study on land use/cover change in loess plateau- A case study of xianyang plateau in shanxi Province," *Arid Zone Research*, vol. 30, no. 03, pp. 563–569, 2013.

[12] R. Hamad, H. Balzter, and K. Kolo, "Predicting land use/land cover changes using a CA-markov model under two different scenarios," *Sustainability*, vol. 10, no. 10, p. 3421, 2018.

[13] G. Herrera-Franco, P. Escandón-Panchana, F. J. Montalván, and A. Velastegui-Montoya, "CLUE-S model based on GIS applied to management strategies of territory with oil wells—case study: santa Elena, Ecuador," *Geography and Sustainability*, vol. 3, no. 4, pp. 366–378, 2022.

[14] G. Chaudhuri and K. Clarke, "The SLEUTH land use change model: a review," *Environmental Resources Research*, vol. 1, no. 1, pp. 88–105, 2013.

[15] V. Equere, P. A. Mirzaei, S. Riffat, and Y. Wang, "Integration of topological aspect of city terrains to predict the spatial distribution of urban heat island using GIS and ANN," *Sustainable Cities and Society*, vol. 69, 2021.

[16] Y. Li, Y. Cai, Q. Fu, X. Zhang, H. Wan, and Z. Yang, "Dynamics of land use/land cover (LULC) considering ecosystem services for a dense-population watershed based on a hybrid dual-subject agent and cellular automaton modeling approach," *Engineering*, 2024.

[17] J. Wu, Z. FengLevin, X. Huang, H. Liu, and L. Huang, "Research on application progress and improvement of CLUE-S model," *Progress in Geographical Science*, vol. 31, no. 1, pp. 3–10, 2012.

[18] C. A. Jantz, S. J. Goetz, D. Donato, and P. Claggett, "Designing and implementing a regional urban modeling system using the SLEUTH cellular urban model," *Computers, Environment and Urban Systems*, vol. 34, no. 1, pp. 1–16, 2010.

[19] Y. Wang, H. Liu, Z. Yu, and L. Tu, "An improved artificial neural network based on human-behaviour particle swarm optimization and cellular automata," *Expert Systems with Applications*, vol. 140, 2020.

[20] D. Valbuena, P. H. Verburg, A. K. Bregt, and A. Ligtenberg, "An agent-based approach to model land-use change at a regional scale," *Landscape Ecology*, vol. 25, no. 2, pp. 185–199, 2010.

[21] M. M. Aburas, Y. M. Ho, B. Pradhan, A. H. Salleh, and M. Y. D. Alazaiza, "Spatio-temporal simulation of future urban growth trends using an integrated CA-Markov model," *Arabian Journal of Geosciences*, vol. 14, no. 2, p. 131, 2021.

[22] X. Fu, X. Wang, and Y. J. Yang, "Deriving suitability factors for CA-Markov land use simulation model based on local historical data," *Journal of Environmental Management*, vol. 206, pp. 10–19, 2018.

[23] F. Moradi, H. S. Kaboli, and B. Lashkarara, "Projection of future land use/cover change in the Izeh-Pyon Plain of Iran using CA-Markov model," *Arabian Journal of Geosciences*, vol. 13, no. 19, p. 998, 2020.

[24] Z. Zhang, B. Hu, W. Jiang, and H. Qiu, "Identification and scenario prediction of degree of wetland damage in Guangxi based on the CA-Markov model," *Ecological Indicators*, vol. 127, 2021.

[25] A. Tariq, J. Yan, and F. Mumtaz, "Land change modeler and CA-Markov chain analysis for land use land cover change using satellite data of Peshawar, Pakistan," *Physics and Chemistry of the Earth, Parts A/B/C*, vol. 128, 2022.

[26] Y. Lee and H. Chang, "The simulation of land use change by using CA-Markov model: a case study of Tainan City, Taiwan," in *Proceedings of the 2011 19th International Conference on Geoinformatics*, pp. 1–4, IEEE, Shanghai, China, June 2011.

[27] Z. Wang, Q. Meng, L. Zhang, D. Hu, and T. Yang, "Simulation and prediction of urban heat island in Haikou based on CA-Markov model," *Journal of University of Chinese Academy of Sciences*, vol. 39, no. 6, pp. 742–753, 2022.

[28] H. Chen, Q. Deng, Z. Zhou, Z. Ren, and X. Shan, "Influence of land cover change on spatio-temporal distribution of urban heat island—a case in Wuhan main urban area," *Sustainable Cities and Society*, vol. 79, 2022.

[29] A. Sharma, H. J. S. Fernando, A. F. Hamlet, J. J. Hellmann, M. Barlage, and F. Chen, "Urban meteorological modeling using WRF: a sensitivity study," *International Journal of Climatology*, vol. 37, no. 4, pp. 1885–1900, 2017.

[30] V. Lara-Fanego, J. A. Ruiz-Arias, D. Pozo-Vázquez, F. J. Santos-Alamillos, and J. Tovar-Pescador, "Evaluation of the WRF model solar irradiance forecasts in Andalusia (southern Spain)," *Solar Energy*, vol. 86, no. 8, pp. 2200–2217, 2012.

[31] D. Carvalho, A. Rocha, M. Gómez-Gesteira, and C. Santos, "A sensitivity study of the WRF model in wind simulation for an area of high wind energy," *Environmental Modelling & Software*, vol. 33, pp. 23–34, 2012.

[32] H. Takebayashi and M. Senoo, "Analysis of the relationship between urban size and heat island intensity using WRF model," *Urban Climate*, vol. 24, pp. 287–298, 2018.

[33] T. Holt and J. Pullen, "Urban canopy modeling of the New York city metropolitan area: a comparison and validation of single- and multilayer parameterizations," *Monthly Weather Review*, vol. 135, no. 5, pp. 1906–1930, 2007.

[34] P. Patel, S. Karmakar, S. Ghosh, and D. Niyogi, "Improved simulation of very heavy rainfall events by incorporating WUDAPT urban land use/land cover in WRF," *Urban Climate*, vol. 32, 2020.

[35] G. Chen, L. Zhao, and A. Mochida, "Urban heat island simulations in guangzhou, China, using the coupled WRF/UCM model with a land use Map extracted from remote sensing data," *Sustainability*, vol. 8, no. 7, p. 628, 2016.

[36] D. Xiao, J. Chen, Z. Chen, and B. Zhang, "Simulation test of the influence of Chengdu fine underlying surface information on urban meteorology," *Meteorological Monthly*, vol. 37, no. 3, pp. 298–308, 2011.

[37] Y. Li, T. Okaze, and A. Mochida, "Prediction of the impacts of urbanization using a new assessment system combining an urban expansion model and WRF-Case study for Guangzhou in China," *Journal of Heat Island Institute International*, vol. 9, p. 2, 2014.

[38] E. Zhao, F. Deng, Z. Li, P. Zheng, Q. Feng, and Y. Han, "Study on the thermal environment of wuhan city based on local climate zones," *Source and Environment in the Yangtze Basin*, vol. 32, no. 5, pp. 1030–1041, 2023.

[39] Q. Huang, J. Huang, X. Yang, C. Fang, and Y. Liang, "Quantifying the seasonal contribution of coupling urban land use types on Urban Heat Island using Land Contribution Index: a case study in Wuhan, China," *Sustainable Cities and Society*, vol. 44, pp. 666–675, 2019.

[40] A. De Meij and J. F. Vinuesa, "Impact of SRTM and Corine Land Cover data on meteorological parameters using WRF," *Atmospheric Research*, vol. 143, pp. 351–370, 2014.

[41] N. Privault, "Understanding Markov chains: examples and applications," in *Springer Undergraduate Mathematics Series*, Springer, Singapore, 2018.

[42] A. F. Koko, W. Yue, G. A. Abubakar, R. Hamed, and A. A. N. Alabsi, "Monitoring and predicting spatio-temporal land use/land cover changes in zaria city, Nigeria, through an integrated cellular automata and Markov chain model (CA-Markov)," *Sustainability*, vol. 12, no. 24, 2020.

[43] S. Deep and A. Saklani, "Urban sprawl modeling using cellular automata," *The Egyptian Journal of Remote Sensing and Space Science*, vol. 17, no. 2, pp. 179–187, 2014.

[44] Q. Jiang, X. Ouyang, Z. Wang, Y. Wu, and W. Guo, "System dynamics simulation and scenario optimization of China's water footprint under different SSP-RCP scenarios," *Journal of Hydrology*, vol. 622, 2023.

[45] D. G. Fox, "Judging air quality model performance: a summary of the ams workshop on dispersion model performance, woods hole, mass., 8–11 september 1980," *Bulletin of the American Meteorological Society*, vol. 62, no. 5, pp. 599–609, 1981.

[46] C. J. Willmott, "Some comments on the evaluation of model performance," *Bulletin America Meteorology Social*, vol. 63, no. 11, pp. 1309–1313, 1982.

[47] F.-Y. Cheng, Y.-C. Hsu, P.-L. Lin, and T.-H. Lin, "Investigation of the effects of different land use and land cover patterns on mesoscale meteorological simulations in the taiwan area," *Journal of Applied Meteorology and Climatology*, vol. 52, no. 3, pp. 570–587, 2013.

[48] A. Jana, M. K. Jat, A. Saxena, and M. Choudhary, "Prediction of land use land cover changes of a river basin using the CA-

Markov model," *Geocarto International*, vol. 37, no. 26, pp. 14127–14147, 2022.

[49] Z. Xu, Y. Han, C.-Y. Tam, Z.-L. Yang, and C. Fu, "Bias-corrected CMIP6 global dataset for dynamical downscaling of the historical and future climate (1979–2100)," *Scientific Data*, vol. 8, no. 1, p. 293, 2021.

[50] H. Zhai, C. Lv, W. Liu et al., "Understanding spatio-temporal patterns of land use/land cover change under urbanization in wuhan, China, 2000–2019," *Remote Sensing*, vol. 13, no. 16, p. 3331, 2021.

[51] L. Díaz-Chávez, R. Melendez-Surmay, and H. A. Arregocés, "Urban heat island intensity in coastal cities of northern Colombia using Landsat data and WRF/UCM model," *Case Studies in Chemical and Environmental Engineering*, vol. 9, 2024.

[52] K. Ezimand, H. Aghighi, D. Ashourloo, and A. Shakiba, "The analysis of the spatio-temporal changes and prediction of built-up lands and urban heat islands using multi-temporal satellite imagery," *Sustainable Cities and Society*, vol. 103, 2024.

[53] M. Kiavarz, S. B. Hosseinbeigi, N. Mijani, M. S. Shahsavary, and M. K. Firozjaei, "Predicting spatial and temporal changes in surface urban heat islands using multi-temporal satellite imagery: a case study of Tehran metropolis," *Urban Climate*, vol. 45, 2022.

[54] M. Mokarram, F. Taripanah, and T. M. Pham, "Investigating the effect of surface urban heat island on the trend of temperature changes," *Advances in Space Research*, vol. 72, no. 8, pp. 3150–3169, 2023.

[55] D. Zhu, X. Zhou, and W. Cheng, "Water effects on urban heat islands in summer using WRF-UCM with gridded urban canopy parameters-A case study of Wuhan," *Building and Environment*, vol. 225, 2022.

[56] S. Yuan, Z. Ren, X. Shan, Q. Deng, and Z. Zhou, "Seasonal different effects of land cover on urban heat island in Wuhan's metropolitan area," *Urban Climate*, vol. 49, 2023.